

Ponomarenko dynamo sustained by a free swirling jet

I. Grants¹ and J. Priede^{1, a)}

*Faculty of Science and Technology, University of Latvia, Riga, LV-1004,
Latvia*

We present numerical results on dynamo action in a flow driven by an azimuthal body force localized near the end of an elongated cylindrical container. The analysis focuses on the central region of the cylinder, where axial variations in the flow are relatively weak, allowing the magnetic field to be represented as a helically traveling wave. Four magnetic impeller configurations and multiple forcing intensities are examined. In all cases, the velocity profiles in the central region display a similar $\propto r^{-2}$ dependence across a wide range of Reynolds numbers and forcing region widths. The magnetic field is found to start growing under conditions similar to those of the Riga dynamo. However, the growing modes exhibit a substantial nonzero group velocity, indicating that the associated instability is convective: the flow can amplify an externally applied magnetic field but cannot sustain it autonomously. We outline several approaches for overcoming this limitation in order to realize a working laboratory dynamo based on an internally unconstrained swirling jet-type flow.

^{a)}Also at Fluid and Complex Systems Research Centre, Coventry University, Coventry, CV1 5FB, UK

I. INTRODUCTION

Screw-like motion of an electrically conducting fluid is arguably the simplest flow capable of sustaining a magnetic field through dynamo action.¹ The most prominent example is the Ponomarenko dynamo,² which can generate a magnetic field at relatively low flow velocities attainable in laboratory conditions.³ This was first demonstrated in the celebrated Riga dynamo experiment^{4,5}, where the flow of liquid sodium was kinematically constrained and guided to mimic the solid-body helical motion of the original Ponomarenko dynamo. An even more constrained configuration was used in the Karlsruhe dynamo experiment, which, however, relied on a different dynamo model, the Roberts-Busse dynamo.⁶ In both cases, the flow had severely restricted freedom to respond to the growing electromagnetic force once the magnetic field reached significant strength. This nonlinear interaction between the flow and the magnetic field – responsible not only for magnetic field saturation but also for potentially complex temporal behavior – is arguably the most scientifically challenging aspect of fluid dynamos.

The aim of the present study is to numerically explore the feasibility of a laboratory screw-type dynamo driven by an impeller in a cylindrical vessel, whose only constraints are the external walls. Previous analysis based on Wentzel-Kramers-Brillouin (WKB) approximation suggests that a smooth swirling-jet flow, which is often referred to as the smooth Ponomarenko dynamo,⁷ may be able to generate a magnetic field at significantly lower velocities than the solid-body Ponomarenko dynamo.⁸ However, the accuracy of the underlying asymptotic solution is uncertain, and the analysis relies on highly idealized velocity profiles.

In the present study, we numerically solve the one-dimensional induction equation for velocity profiles that approximate a concentrated vortex driven by a small-diameter impeller in a finite cylinder. A striking and well-known example of such a flow is produced by a laboratory magnetic bar stirrer.⁹ A similar vortex flow can also be generated by azimuthal electromagnetic body forces arising from a rotating permanent magnet placed coaxially near the cylinder's end wall.¹⁰ We use direct numerical simulations to compute several representative realizations of such flows, which then serve as input for the induction equation within the smooth Ponomarenko dynamo framework.

The flow described above may enable a technically simple implementation of a liquid-metal laboratory dynamo using a commercially manufactured large sodium storage tank,

which can contain up to 22 m^3 of liquid sodium. In the simplest realization, the flow could be driven in an unmodified tank by a rotating permanent magnet. Alternatively, the flow could be generated by a mechanically driven impeller, actuated either through a sealed shaft or by magnetic coupling.

The considered configuration shares strong similarities with the Riga dynamo.^{4,5} The primary distinction is the absence of internal walls, which results in smooth radial velocity profiles. Eliminating these walls simplifies the experiment by removing the requirement for reliable electrical contact across them. It also relaxes kinematic constraints on how the flow can respond to the generated magnetic field. Consequently, the proposed configuration may be advantageous for studying strongly nonlinear regimes well above the dynamo threshold.

Another important difference concerns the direction of the axial flow relative to the agitator. In the Riga dynamo, a propeller pushes the liquid sodium axially. In contrast, in our setup, the impeller produces a centrifugal radial jet while simultaneously drawing axial flow toward itself. At the opposite end of the cylinder, a flow topology forms that resembles a tornado or, to a lesser extent, an accretion disk with polar jets. These distinctions, however, do not alter the fundamental generation mechanism of the magnetic field by the helical vortex core.

The flow in the von Kármán sodium (VKS) dynamo experiment¹¹ is driven by two relatively large-diameter impellers. The liquid-metal vessel has a diameter nearly equal to its height, and the impellers counter-rotate. The design philosophy of the VKS experiment emphasizes strong turbulence rather than screw-like coherent motion. As a result, both the flow structure and the overall dynamo concept differ substantially from the Ponomarenko-type dynamo considered here.

The paper is organized as follows. In the next section, we introduce the mathematical model and briefly describe the numerical method, which is based on the Chebyshev-tau approximation. Results of the direct numerical simulations of the impeller-driven flow are presented in Sec. III A, and these velocity fields are then used in Sec. III B to determine the threshold of dynamo action by numerically integrating the induction equation. The paper concludes with a discussion of the results in Sec. IV.

II. MODEL

We consider a swirling flow of an incompressible fluid with electrical conductivity σ , which is driven by an impeller in a finite-length cylinder of radius R_0 and focus on the middle part of the cylinder, where the axial variation of the flow is relatively small. The cylinder is surrounded by an electrically insulating medium, and the impeller is modeled by an axially symmetric azimuthal body force distribution representing the time-averaged action of a rotating permanent magnet placed coaxially near one end of the cylinder.

Following the classical kinematic dynamo approach, the magnetic field is supposed to be generated by the mean flow, with turbulent fluctuations playing no significant role in this process. The flow is represented in cylindrical coordinates (r, ϕ, z) by an axially and rotationally invariant velocity profile $\mathbf{v}(r) = \mathbf{e}_\phi r\Omega(r) + \mathbf{e}_z W(r)$, which is obtained by averaging the time-dependent 3D numerical solution of the Navier-Stokes equation.

Using R_0 and $\mu_0\sigma R_0^2$ as the length and time scales, the induction equation for the magnetic field $\mathbf{B}(\mathbf{r}, t)$ in the cylinder can be written in the following dimensionless form

$$\partial_t \mathbf{B} = Rm \nabla \times (\mathbf{v} \times \mathbf{B}) + \nabla^2 \mathbf{B}, \quad (1)$$

where $Rm = \mu_0\sigma R_0 V_0$ is the magnetic Reynolds number based on the maximal axial velocity V_0 , which corresponds to $\max_r |W(r)| = 1$ in the dimensionless form. As \mathbf{v} depends only on r , particular solutions of the magnetic field can be sought as the normal mode

$$\mathbf{B}(r, \phi, z, t) = \hat{\mathbf{B}}(r, t) e^{i(kz + m\phi)} + \text{c.c.}, \quad (2)$$

with a complex time-dependent radial amplitude distribution $\hat{\mathbf{B}}(r, t)$. The magnetic field is completely determined by any two of its components due to solenoidality. In our case, it is advantageous to employ the radial and azimuthal components as the independent variables. Combining the respective components of Eq. (1), it can be written in the following compact form:

$$\partial_t \hat{B}_\pm = [D_{m\pm 1} - k^2 - iRm(m\Omega + kW)] \hat{B}_\pm \pm iRmr\Omega'(\hat{B}_+ + \hat{B}_-)/2, \quad (3)$$

where $\hat{B}_\pm = \hat{B}_r \pm i\hat{B}_\phi$ and $D_m = \frac{d^2}{dr^2} + \frac{1}{r} \frac{d}{dr} - m^2 r^{-2}$. Outside the cylinder ($r > 1$), where $\sigma = 0$, the induction equation reduces to $D_{m\pm 1} \hat{B}_\pm = 0$ and has an analytical solution:

$$\hat{B}_\pm(r) = A_\pm K_{m\pm 1}(kr),$$

where $K_m(x)$ is the modified Bessel function of the second kind and A_{\pm} are two unknown constants. The irrotationality of the free-space magnetic field results in $A_+ = A_-$. Using this analytic solution and the continuity of the magnetic field, we obtain the two boundary conditions for \hat{B}_{\pm} expressed as

$$\hat{B}_+ - \gamma \hat{B}_- = 0, \quad (4)$$

$$\hat{B}'_+ + \hat{B}'_- + s \hat{B}_- = 0, \quad (5)$$

where $\gamma = K_{m+1}(k)/K_{m-1}(k)$ and $s = \gamma(m+1) - (m-1) + (\gamma-1)k^2/m$. The last condition results from the continuity of the axial component of the magnetic field and ensures that no electric current flows through the cylinder boundary at $r = 1$. At the axis ($r = 0$), for $m = 1$ considered in the following, we have the pole condition

$$\hat{B}_+ = 0, \quad (6)$$

which follows from the single-valuedness of the magnetic field. The formulation of the problem above is equivalent to the one used by Dobler *et al.*¹²

Equations (3) are integrated over time numerically using the Adams-Bashforth method, which results in a system of two ordinary differential equations

$$D_{m\pm 1} \hat{B}_{\pm}^{n+1} - (k^2 + 1.5/\Delta t) \hat{B}_{\pm}^{n+1} = 2F_{\pm}^n - F_{\pm}^{n-1} - (2\hat{B}_{\pm}^n - 0.5\hat{B}_{\pm}^{n-1})/\Delta t, \quad (7)$$

where $\hat{B}_{\pm}^n(r) = \hat{B}_{\pm}(r, t_n)$, $\Delta t = t_{n+1} - t_n$, and F_{\pm} represent the convective terms with Rm in Eq. (3). The problem is solved numerically using the Chebyshev tau approximation, where for $m = 1$ the solution is sought as a series of even Chebyshev polynomials

$$\hat{B}_{\pm}^n(r, t_n) = \sum_{i=0}^N b_i^{\pm}(t_n) T_{2i}(r), \quad (8)$$

with unknown time-dependent coefficients $b_i^{\pm}(t_n)$. This series contains only even Chebyshev polynomials because of the axial reflection symmetry, which implies \hat{B}_{\pm} for mode $m = 1$ to be even functions of r .

Substituting (8) into (7) and using the orthogonality of Chebyshev polynomials, we obtain two sets of $N + 1$ linear algebraic equations for b_i^{\pm} . The equations are modified by the

boundary conditions (4,5), which take the form:

$$\sum_{i=0}^N (b_i^+ + \gamma b_i^-) = 0, \quad (9)$$

$$\sum_{i=0}^N (4i^2(b_i^+ + b_i^-) + sb_i^-) = 0. \quad (10)$$

According to the tau method, these boundary conditions override the last two algebraic equations for b_i^\pm , which are produced by the projection of (7) onto $T_{2N}(r)$. Likewise, the second to last equation for b_i^+ is overridden by the pole condition (6), which takes the form:

$$\hat{B}_+ \Big|_{r=0} = \sum_{i=0}^N (-1)^i b_i^+ = 0. \quad (11)$$

Note that there is another pole condition $\hat{B}'_- = 0$ at $r = 0$, which is satisfied by (8) automatically.

Computations are carried out using the spatial resolution $N = 96$ and the time step $\Delta t = 0.01Rm^{-1}$, starting from the initial state $\hat{B}_+ = 0$ and \hat{B}_- , defined by three non-zero coefficients $b_{0,1,2}^- = (3, -4, 1)/6$, which satisfy the boundary conditions (4,5) at $t = 0$, as both \hat{B}_- and its radial derivative are zero at $r = 1$. The leading eigenvalue is computed using the Goldhirsch method¹³ based on five trailing snapshots, each separated by 20 time steps. The calculation proceeds until the change in the leading eigenvalue between successive iterations falls below 0.01%. Accuracy to three decimal places is verified by repeating the computation with twice the temporal resolution and with $N = 128$.

The code was validated by solving a test problem for $k = 2$ and

$$\Omega(r) = -2W(r) = Rm(1 - \tanh(\alpha(r - 1/2))).$$

The critical value $Rm = 41.3$ agrees almost perfectly with the analytical result $Rm = 41.32$ for the classical Ponomarenko dynamo, which corresponds to the limit $\alpha \rightarrow \infty$. The oscillation frequency at onset was 17.55 and 17.85 for $\alpha = 20$ and 50, respectively, corresponding to deviations of 2.2% and 0.5% from the analytical value 17.94.

The velocity profiles $\Omega(r)$ and $W(r)$ are obtained by direct numerical simulation (DNS) using the spectral code described by Grants¹⁰. This code solves the three-dimensional, transient, incompressible Navier-Stokes equations in a cylindrical domain with a prescribed body force. The force is generated either by a coaxial, radially magnetized rotating cylindrical

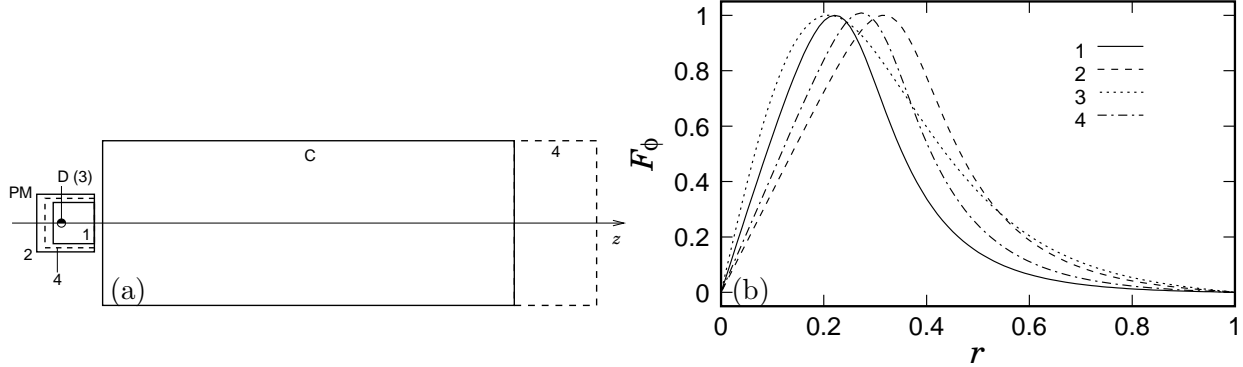


FIG. 1. Schematic of the four numerically simulated configurations (a) and the corresponding radial profiles of the azimuthal body force at the magnet-facing surface (b). The flow in the liquid cylinder (C) is driven either by a rotating permanent magnet (PM) or by a rotating magnetic dipole (D). The cylinder has a length-to-diameter ratio of 2.5 in cases 1–3 and 3.0 in case 4 (shown with dashed lines). The permanent magnet has a diameter and length equal to 0.25 and 0.35 cylinder diameters in cases 1 and 2, respectively, and 0.3 cylinder diameters in case 4. The gap between the PM and the liquid is 0.05 cylinder diameters. In case 3, the dipole is positioned 0.25 cylinder diameters away from the liquid.

permanent magnet or by a rotating magnetic dipole. Its spatial distribution is computed by neglecting both the skin effect and the influence of the flow.¹⁴

The core flow described by $\Omega(r)$ and $W(r)$ is weakly affected by the distribution of the driving body force because the two are spatially separated. Specifically, the body force is negligible in the central part of the cylinder, where the flow is primarily shaped by vortex stretching resulting from the centrifugal action of the impeller. The magnet arrangement in the four configurations is shown schematically in Fig. 1(a). The chosen aspect ratio of the cylindrical container is close to that of commercial sodium storage tanks.

Time-averaged distributions of driving force are computed using the analytical expressions from Berenis and Grants¹⁴ and are displayed in Fig. 1(b), with maxima scaled to unity. The flow is time-averaged over approximately 50 vortex core revolutions, following an initial transient of comparable duration.

Simulations are performed with a spatial resolution of $97 \times 97 \times 109$ modes. To evaluate the influence of numerical parameters, velocity profiles are also computed using a coarser resolution of $83 \times 83 \times 97$ modes. The temporal resolution corresponds to approximately

5000 time steps per vortex-core revolution.

III. RESULTS

A. Velocity field

Time-averaged velocity distributions were computed numerically using a constant azimuthal body force with the radial profiles shown in Fig. 1(b). The force distribution was multiplied by a dimensionless factor, chosen to be as large as possible while still yielding numerically reliable velocity distributions. The numerical error was estimated by comparing the z -averaged velocity profiles obtained at two spatial resolutions ($97 \times 97 \times 109$ and $83 \times 83 \times 97$ modes). The difference between these profiles was less than 5% of the corresponding maximum value when the flow Reynolds number, based on the maximum absolute velocity and the cylinder radius, was 2110, 1660, 1400, and 2120 in cases 1–4, respectively.

Figure 2 shows a representative distribution of angular and axial velocity. In all four cases, the distributions showed a similar degree of axial non-uniformity in the middle half of the cylinder, the region over which the velocity profiles were averaged. Axial variations were most pronounced in case 4, which involved a longer cylinder with a diameter-to-height ratio of 0.33. The mean radial velocity in the central region of the cylinder was negligible in all cases.

Figure 3 shows the velocity profiles averaged over z in the middle half of the cylinder and scaled by the maximum absolute axial velocity. The axial velocity profiles are remarkably similar despite the significantly different forcing distributions and the variations in the Reynolds number. Outside the boundary layer at the side wall ($r = 1$), all four numerically computed profiles are well approximated by the following expressions

$$\Omega(r) = ab g(ar), \quad (12)$$

$$W(r) = \frac{g(cr) - d}{d - 1}, \quad (13)$$

where $g(x) = (1 + x^2)^{-1}$ and a, b, c are free parameters with $d = \ln(1 + c^2)/c^2$ ensuring a zero net flow rate $\int_0^1 W(r)r dr = 0$.

B. Dynamo

In this section, we numerically simulate the temporal evolution of the magnetic field in the four flow configurations whose velocity profiles are shown in Fig. 3. We use the ‘snapshot’ method¹³ to determine the leading eigenvalue λ for the normal mode of the magnetic field (2) with $m = 1$ by integrating over time the induction equation (3) with computed velocity profiles for various magnetic Reynolds numbers Rm and axial wavenumbers k . The marginal Rm , by exceeding which the magnetic field mode with the axial wavenumber k starts to grow exponentially at a rate $\Re(\lambda) > 0$, is plotted in Fig. 4(a). The imaginary part of the leading eigenvalue, $\Im(\lambda) = \omega$, defining the frequency with which the magnetic field oscillates in time at this point, is shown in Fig. 4(b). The lowest point on each marginal Rm curve defines the critical magnetic Reynolds number, Rm_c , at which the given flow becomes able to sustain a magnetic field with the corresponding wavenumber and frequency. Critical parameters computed for the velocity profiles obtained by DNS are summarized in Table II along with the results for the corresponding best-fit profiles Eq.(12). For the fitted profiles, the critical magnetic Reynolds numbers Rm_c are about 15–50% higher than those for the DNS counterparts. The fitted velocity profiles also produce slightly larger critical wavenumbers k_c and frequencies ω_c . Small variations in the velocity profiles (Fig. 3) are seen to cause much bigger variations in Rm_c , demonstrating the strong sensitivity of the dynamo threshold to the velocity field.

Note that the marginal modes of the magnetic field, which by definition have a zero temporal growth rate $\Re(\lambda) = 0$, generally have a non-zero frequency $\Im(\lambda) = \omega$. As seen in Fig. 4, this frequency is not constant but varies with the wavenumber k . As a result, the modes have not only a non-zero phase velocity ω/k , but also a non-zero group velocity $\partial_k \omega$. Note that the latter is the velocity of the wave packet made up of a superposition of modes

TABLE I. Fitted parameters of the velocity profiles for the four numerically simulated cases.

	<i>a</i>	<i>b</i>	<i>c</i>
1	3.22	2.06	2.01
2	3.00	2.50	1.65
3	2.95	2.12	1.82
4	2.75	2.11	1.63

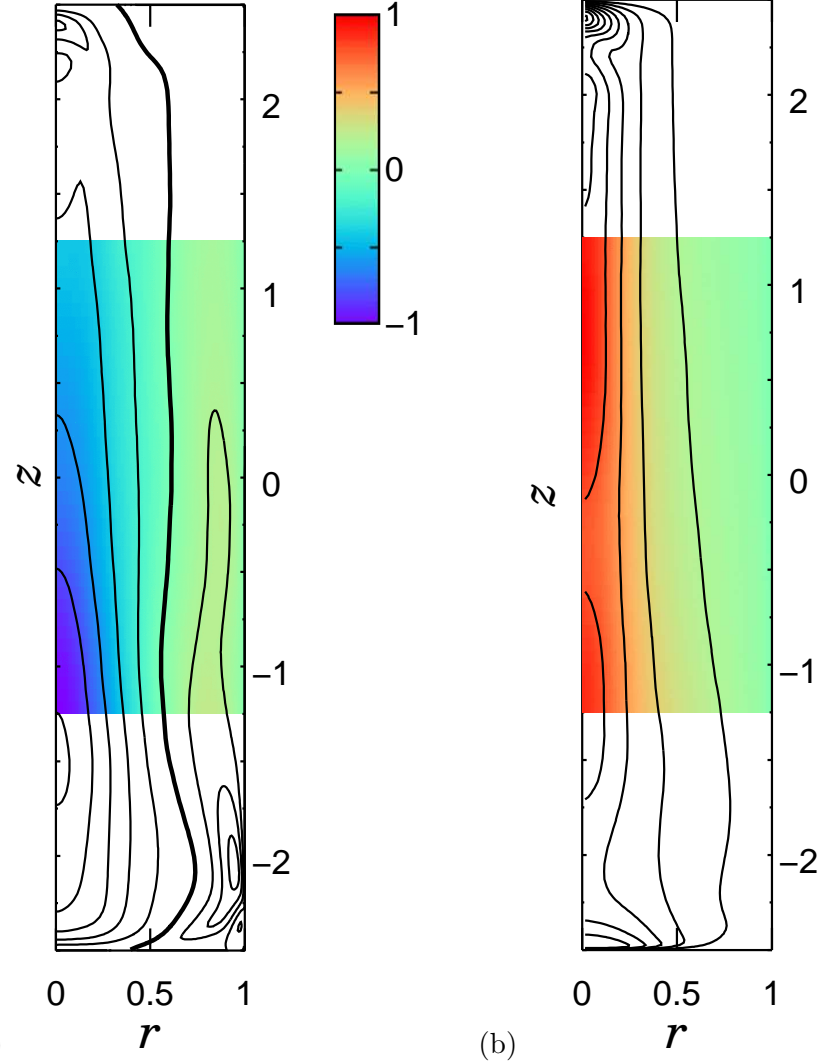


FIG. 2. Axial (a) and angular (b) velocity distributions for case 1. Colors are superimposed in the central half of the cylinder, over which the profiles in Fig. 3 are averaged. The isoline interval is 0.2 times the corresponding maximum absolute value in the averaging domain.

centered around k . Such a growing wave packet of the modes centered around k_c emerges as soon as Rm exceeds Rm_c . When this wave packet with the growing magnetic field travels along the cylinder with a non-zero group velocity, the magnetic field grows only in the co-moving frame of reference, eventually decaying at any fixed position. For the magnetic field to persist in the laboratory (fixed) frame of reference, the group velocity of the critical mode must be zero. This means that, at the critical wavenumber k_c , where marginal Rm attains its minimum and thus $\partial_k Rm = 0$, we also need $\partial_k \omega = 0$, which implies a local extreme of ω at the same point.

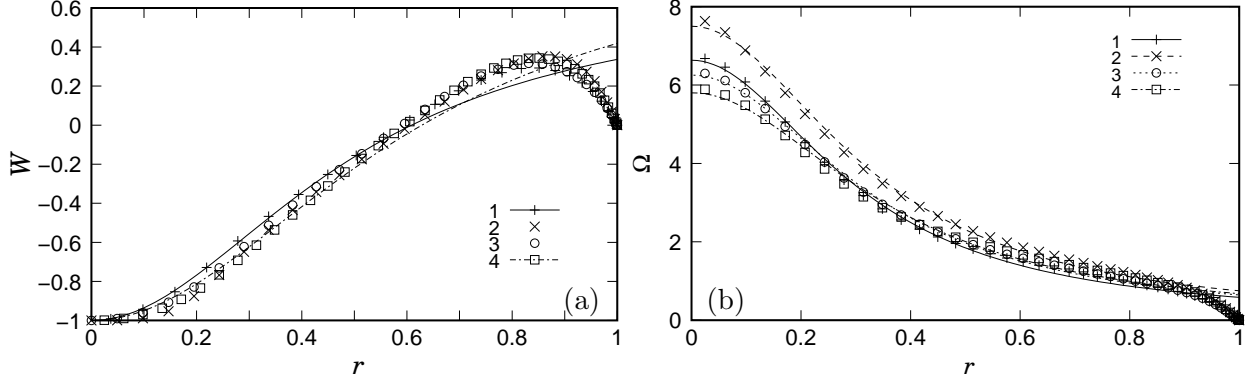


FIG. 3. Axial (a) and angular (b) velocity profiles averaged over z in the central half of the cylinder. The numbers in the legend correspond to the cases shown in Fig. 1. The velocity profile fits defined by Eq. (12) are shown as curves, and the corresponding fit parameters are listed in Table I.

Numerical results show that $\omega(k)$ has a maximum that is slightly offset from that of $Rm(k)$. This means that the critical mode has a non-zero group velocity $v_g = \partial_k \omega / Rm$. Adding this v_g to the axial velocity profile $W(r) + v_g$ shifted the maximum of ω to k_c .

When the marginal Rm is represented parametrically as a function of the marginal frequency $\omega(k) : Rm = Rm(\omega(k))$, at the point of absolute instability, where $\partial_k Rm = \partial_k \omega = 0$ and $\omega_c = \omega(k_c)$, we have

$$\partial_\omega Rm = \partial_k Rm / \partial_k \omega = \partial_k^2 Rm / \partial_k^2 \omega.$$

As this point is a minimum of Rm , in general, we have $\partial_k^2 Rm > 0$ and, thus, according to the relation above $\partial_\omega Rm \neq 0$. This non-zero derivative, in turn, means that the marginal $Rm(\omega(k))$ curve at the minimum has a cusp – a singularity in the form of a sharp peak with coincident tangents.¹⁵ This is a characteristic feature of absolute instability, which was originally identified in the complex frequency plane.¹⁶ When a uniform back-flow exceeding the group velocity is added to the axial velocity profile, the cusp morphs into a closed loop with a self-intersection point on the marginal $Rm(\omega(k))$ curve. This self-intersection point is a prerequisite of absolute instability at complex wave numbers.¹⁷ Our current results show such an intersection point (Fig. 5), and thus absolute instability appears only at sufficiently strong additional back-flow.

Figure 6 shows the radial profile of the critical magnetic-field mode for case 1. The field reaches its maximum amplitude at $r \approx 0.4$ and decreases to nearly zero at the cylinder boundary, $r = 1$. A similar radial distribution is found for all other cases. The low magnitude

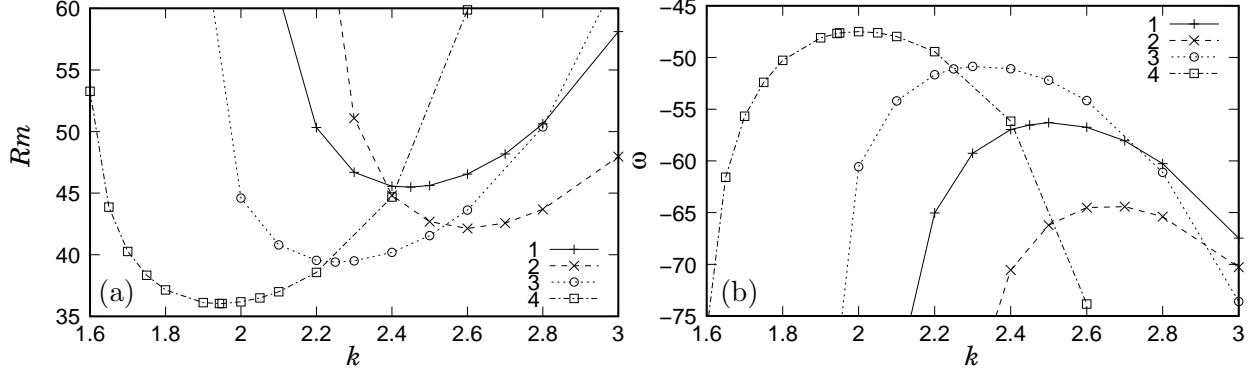


FIG. 4. Magnetic Reynolds number (a) and oscillation frequency (b) of marginal modes of the magnetic field versus axial wavenumber k and $m = 1$ for the four velocity profiles corresponding to the configurations shown in Fig. 1.

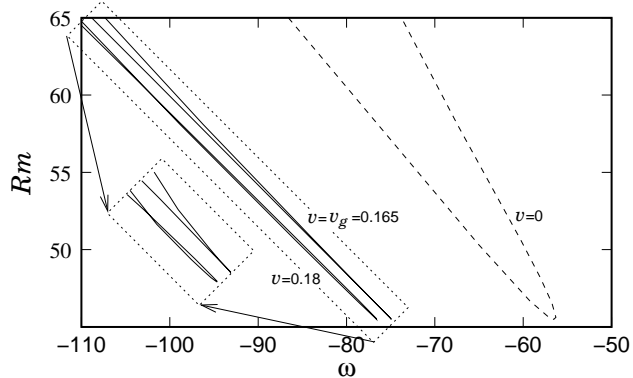


FIG. 5. The marginal Rm as a function of marginal frequency ω for case 1 with a uniform back-flow v .

of the critical mode at the boundary $r = 1$ makes it an almost invisible dynamo. The invisible dynamo produces no magnetic field outside the conducting domain.¹⁸ This study¹⁸ sought an invisible dynamo in an infinite cylinder and only decaying invisible modes have been observed. Instead of requiring strictly invisible dynamo one could look for a velocity field that generates magnetic field with a possibly low magnitude at the boundary (relative to interior). Our results suggest that such weak formulation might produce practically meaningful results.

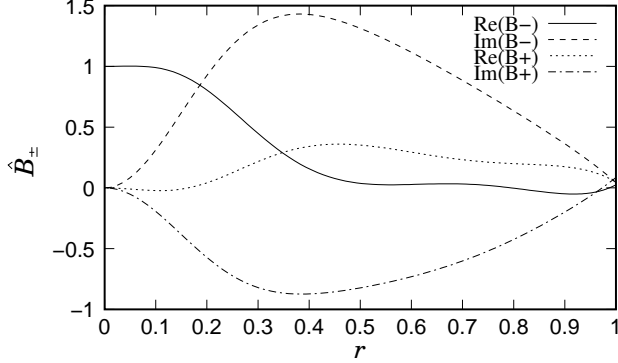


FIG. 6. The critical mode of the magnetic field for case 1 normalized so that $\hat{B}_-(0) = 1$.

TABLE II. Threshold parameters in the four numerically simulated cases. The asterisk denotes the results obtained using the corresponding best-fit velocity profiles (12).

	Rm_c	k_c	ω_c	v_g	Rm_c^*	k_c^*	ω_c^*
1	45.5	2.45	-56.5	0.165	52.9	2.84	-59.9
2	42.1	2.60	-64.5	0.188	64.0	3.02	-91.4
3	39.4	2.25	-51.1	0.182	47.7	2.59	-57.3
4	36.0	1.95	-47.6	0.190	44.1	2.33	-53.6

IV. DISCUSSION

This study shows that an impeller-driven liquid sodium flow in a cylinder can reach the convective instability threshold for the generation of a magnetic field. For instance, the critical magnetic Reynolds number $Rm_c = 36$ found for the fourth considered flow configuration corresponds to $V_0 \approx 5.4$ m/s in a 4 m^3 liquid sodium tank with a diameter $2R_0 \approx 1.2$ m and 3:1 length-to-diameter ratio. This is somewhat lower than the velocity in the Riga dynamo of similar length, which used about 1.5 m^3 of sodium. In a 22 m^3 tank, we expect the critical velocity to be below 3 m/s, which should allow the setup to reach a strongly supercritical dynamo regime.

However, these results are not fully conclusive because they are based on a highly idealized model of an infinitely long cylinder. In this model, the growing magnetic field propagates along the cylinder with a non-zero group velocity, which is characteristic of a convective instability. This means that although the flow can amplify the magnetic field, it cannot

sustain it indefinitely because the field eventually escapes through the end of the cylinder.

Several approaches may help to overcome this limitation. First, only a few representative configurations have been explored here. At least two geometric parameters can be tuned: the cylinder aspect ratio and the impeller-to-cylinder diameter ratio. Additional parameters arise when the flow is driven by a mechanical impeller. These degrees of freedom may allow for a configuration in which the group velocity vanishes. The velocity profile approximation (12) is well suited for such a search. In this parametrization, a and c characterize the widths of the angular and axial core velocity profiles, respectively, while b defines the pitch of the helical core flow.

The convective instability can, in principle, be made self-sustained by magnetically coupling the two ends of the cylinder so that the growing magnetic field arriving at one end is fed back to the other end. Such a mechanism could be realized, for example, by means of an external coil system. A conceptually similar approach was proposed by Bourgoin *et al.*¹⁹, where an additional amplifier was incorporated into an electrical feedback loop.

Another possibility is to employ a second, identical cylinder placed side by side. If the axial flows in the two cylinders are directed oppositely, the combined system would possess no preferred axial direction. Magnetic coupling through the ends of the cylinders could then provide the necessary feedback without significantly increasing the critical magnetic Reynolds number Rm .

A further potential mechanism relies on the radially converging boundary layer, which may supply the feedback required to sustain amplification by the core helical flow. Such coupling may be facilitated by the relatively short axial wavelength of the marginal magnetic mode: in all four simulated cases, approximately two full critical wavelengths fit within the cylinder. If effective, such feedback could be captured by two-dimensional dynamo model in a finite cylinder^{20,21} with vacuum magnetic boundary conditions. Two-dimensional modeling would also clarify influence of the magnetic boundary conditions at the ends of a finite-length cylinder.

The convective nature of the dynamo is not the only potential obstacle to realizing the considered configuration as a working laboratory set-up. Our results indicate that the amplification of the magnetic field is sensitive to relatively small variations in the velocity profile. The present simulations were performed at hydrodynamic Reynolds numbers of 1000–2000, which effectively corresponds to an unrealistically large magnetic Prandtl number of order

0.02. In reality, the velocity distributions may differ substantially from those obtained here.

Nevertheless, the observed $\propto r^{-2}$ dependence should remain robust, at least for the angular velocity profile, because it follows directly from angular momentum conservation in a stretched vortex. The axial velocity profile is influenced in part by Ekman pumping in the radially converging boundary layer. For this reason, an approximate $\propto r^{-2}$ scaling may also hold in the axial velocity component at much higher Reynolds numbers. Moreover, the axial uniformity of the bulk flow is expected to improve with increasing Reynolds number due to the Taylor–Proudman theorem. Thus, the core velocity field is likely to retain the general form (12), parameterized by three characteristic scales.

Among these, the pitch of the helical core flow, b^{-1} , appears particularly important. Our DNS results yielded pitch values around 0.5, which are significantly smaller than the optimal value ≈ 1.3 for the classical Ponomarenko dynamo³. The pitch is likely to be even lower under realistic turbulent sodium flow conditions, in which case the critical magnetic Reynolds number Rm_c could become prohibitively large for laboratory realization. The observed sensitivity of Rm_c to velocity profile shape requires accurate velocity measurements at relevant hydrodynamical conditions as an important first step towards the laboratory dynamo. If a too small core pitch value is measured, then the magnetic impeller could be replaced by a mechanical impeller specifically designed to enhance axial flow. In practice, this could be implemented with a propeller operated in reverse, driving axial flow toward the adjacent end wall.

AUTHOR DECLARATIONS

Conflict of Interest

The authors have no conflicts to disclose.

Data availability

The data that support the findings of this study are available from the corresponding author upon reasonable request.

REFERENCES

¹D. Lortz, “Exact solutions of the hydromagnetic dynamo problem,” *Plasma Phys.* **10**, 967 (1968).

²Y. B. Ponomarenko, “Theory of the hydromagnetic generator,” *J. Appl. Mech. Tech. Phys.* **14**, 775–778 (1973).

³A. Gailitis and J. Freibergs, “Theory of a helical MHD dynamo,” *Magnetohydrodynamics* **12**, 127–130 (1976).

⁴A. Gailitis, O. Lielausis, S. Dementev, E. Platacis, A. Cifersons, G. Gerbeth, T. Gundrum, F. Stefani, M. Christen, H. Hänel, and G. Will, “Detection of a flow induced magnetic field eigenmode in the Riga dynamo facility,” *Phys. Rev. Lett.* **84**, 4365–4368 (2000).

⁵A. Gailitis, O. Lielausis, E. Platacis, S. Dementev, A. Cifersons, G. Gerbeth, T. Gundrum, F. Stefani, M. Christen, and G. Will, “Magnetic field saturation in the Riga dynamo experiment,” *Phys. Rev. Lett.* **86**, 3024 (2001).

⁶R. Stieglitz and U. Müller, “Experimental demonstration of a homogeneous two-scale dynamo,” *Phys. Fluids* **13**, 561–564 (2001).

⁷A. D. Gilbert, “Dynamo theory,” in *Handbook of mathematical fluid dynamics*, Vol. 2 (Elsevier, 2003) pp. 355–441.

⁸A. Ruzmaikin, D. Sokoloff, and A. Shukurov, “Hydromagnetic screw dynamo,” *J. Fluid Mech.* **197**, 39–56 (1988).

⁹G. Halász, B. Gyüre, I. M. Jánosi, K. G. Szabó, and T. Tél, “Vortex flow generated by a magnetic stirrer,” *Am. J. Phys.* **75**, 1092–1098 (2007).

¹⁰I. Grants, “Rotating magnetic dipole-driven flows in a conducting liquid cylinder,” *Phys. Fluids* **33** (2021).

¹¹R. Monchaux, M. Berhanu, S. Aumaître, A. Chiffaudel, F. Daviaud, B. Dubrulle, F. Ravelet, S. Fauve, N. Mordant, F. Pétrélis, M. Bourgoin, P. Odier, J.-F. Pinton, N. Plihon, and R. Volk, “The von Kármán Sodium experiment: Turbulent dynamical dynamos,” *Phys. Fluids* **21**, 035108 (2009).

¹²W. Dobler, P. Frick, and R. Stepanov, “Screw dynamo in a time-dependent pipe flow,” *Phys. Rev. E* **67**, 056309 (2003).

¹³L. Goldhirsch, S. A. Orszag, and B. K. Maulik, “An efficient method for computing leading eigenvalues and eigenvectors of large asymmetric matrices,” *J. Sci. Comput.* **2**,

33–58 (1987).

¹⁴D. Berenis and I. Grants, “Analytical induced force solution in conducting cylindrical bodies and rings due to a rotating finite permanent magnet,” *J. Magn. Magn. Mater.* **497**, 165856 (2020).

¹⁵J. Priede and G. Gerbeth, “Absolute versus convective helical magnetorotational instability in a Taylor-Couette flow,” *Phys. Rev. E* **79**, 046310 (2009).

¹⁶K. Kupfer, A. Bers, and A. K. Ram, “The cusp map in the complex-frequency plane for absolute instabilities,” *Phys. Fluids* **30**, 3075–3082 (1987).

¹⁷J. Priede and G. Gerbeth, “Convective, absolute, and global instabilities of thermocapillary-buoyancy convection in extended layers,” *Phys. Rev. E* **56**, 4187 (1997).

¹⁸J. Šimkanin and A. Tilgner, “Inverse dynamo problem in a cylinder,” *Geophys. Astro. Fluid* **102**, 205–215 (2008).

¹⁹M. Bourgoin, R. Volk, N. Plihon, P. Augier, P. Odier, and J.-F. Pinton, “An experimental Bullard–von Kármán dynamo,” *New J. Phys.* **8**, 329 (2006).

²⁰F. Stefani, G. Gerbeth, and A. Gailitis, “Velocity profile optimization for the riga dynamo experiment,” in *Transfer Phenomena in Magnetohydrodynamic and Electroconducting Flows: Selected papers of the PAMIR Conference held in Aussois, France 22–26 September 1997*, edited by A. Alemany, P. Marty, and J.-P. Thibault (Kluwer Academic Publishers, 1999) pp. 31–44.

²¹M. Xu, F. Stefani, and G. Gerbeth, “The integral equation approach to kinematic dynamo theory and its application to dynamo experiments in cylindrical geometry,” *J. Comput. Phys.* **227**, 8130–8144 (2008).